

# Automatic Patency Discrimination in the Pig Bilateral Femoral Veins for Biomedical Implants

Michael A. Rothfuss Michael L. Gimbel Ervin Sejdic

**Abstract**—Free flap surgeries require hourly monitoring to detect vascular compromise. If not caught promptly, the flap can be lost. Monitoring free flaps using the gold standard requires experienced operators to interpret blood flow signatures, which are often difficult to distinguish from background noise. Previously reported hardware-only automatic patency classification showed a high sensitivity, specificity, and a low false-positive rate, but it was demonstrated using bulky discrete electronics and a syringe pump to generate the expected flow rates. In this paper, we investigate automatic hardware-only patency classification on blood flow data collected from the bilateral femoral veins during flow and occluded states using SPICE simulations in an IBM 130 nm CMOS process with a 1-V supply voltage and a 200 ms window length. Experimental results show a very high sensitivity (99.45%), specificity (99.93%), and very low false-positive rate (0.07275%) at just 8.715  $\mu\text{A}$ . This work shows that automatic hardware-only patency classification is effective for monitoring patency on real pig blood flow data. The demonstrated classifier’s performance makes it suitable for integration as part of a wirelessly-powered biomedical patency monitor.

**Keywords:** biomedical monitoring, blood flow, feature classification, free flap, patency

## I. INTRODUCTION

The first several days after a free flap surgery are critical to the survival of the transferred tissue. Typically, hourly monitoring is used to catch loss of flow through the flap early [1]. Otherwise, free flap complications, which occur in up to 10% of cases [2], result in loss of the flap [3] and increased morbidity [4]. Even with frequent monitoring, the gold standard, the Cook-Swartz implantable Doppler probe and system, suffers from high false-positive rates (i.e., up to 31% for head and neck cases [5]). These false-positive rates result in

unnecessary surgical re-exploration of the flaps that cost hospitals \$20k–\$30k for each event [6].

The reason why the gold standard has such a high false-positive rate is because of its transcutaneous wire tether that connects the monitoring probe, which is affixed to the vessel, through the patient’s skin to a bedside monitor. At the end of the monitoring period, the tether is lightly tugged to separate it from the implanted probe, which is left permanently inside the patient [7]. During the first several days of the post-operative period, the tether can be snagged, which can result in damage to the vessel, or it can become dislodged thereby separating the tether from the probe prematurely, which results in loss of signal. Additionally, monitoring venous outflow from the free flap is often preferred to arterial monitoring, because venous flow provides immediate feedback of the flap patency [8]. The problem with monitoring venous flow with the gold standard, especially in the peripheral veins in the legs, is that the flow signature is often very similar to the background noise where there is no flow, requiring experienced operators to correctly identify the existence of flow [9]. Previously, we investigated wireless implantable blood flow monitors in pigs to demonstrate a tether-less patency monitor with an easy-to-interpret operator interface [10]. However, in that work, the implant relied on externally processing the blood flow data before operator assessment, resulting in large and power-hungry high-performance implanted electronics. And still, the technology required the operator to record the baseline no-flow waveform and visually compare it to subsequent flow measurements. In order to completely eliminate operator involvement and to tailor the implanted electronics to the specific application to reduce implant bulk and power consumption, we previously investigated automatic patency classifiers for venous flow rates expected in free flap breast reconstruction surgeries [11].

In this paper, we investigate automatic patency detection on pig blood flow data collected from our previous study [10]. This research builds off of our prior work

Michael A. Rothfuss and Ervin Sejdic are with the Department of Electrical and Computer Engineering, Swanson School of Engineering, University of Pittsburgh, Pittsburgh, PA, USA. E-mails: mar28@pitt.edu, esejdic@ieee.org

Michael L. Gimbel is with the Department of Plastic Surgery, University of Pittsburgh, Pittsburgh, PA, USA. E-mail: gimbelml@upmc.edu.

on automatic patency detection, which was demonstrated using discrete commercial off-the-shelf (COTS) components, and it was evaluated using a syringe pump to generate laminar flow (i.e., venous flow) – not real blood flow data. The COTS classifier from our previous work was adapted from Gestner et al.’s work in automatic analog glass break detectors [12] to operate with blood flow signals. The eventual purpose of our prior work in automatic classifiers was to incorporate it as part of a biomedical implant, specifically as a monolithic integrated circuit. This research’s main contribution is that automatic patency classification has only been demonstrated with COTS parts and using a syringe pump to approximate blood flow rates in free flaps veins [11]. This paper investigates the monolithic implementation of our previous automatic classifier on real pig venous blood flow data with SPICE simulations in an IBM 130 nm CMOS process. A review on wireless totally implantable blood flow monitor miniaturization by Rothfuss et al. [13] concluded that in order to move this technology closer to the ideal free flap monitor described by Smit et al. [14], future designs need to exploit the highly integrated capabilities of monolithic integrated circuitry. A smaller implant would significantly reduce bioburden and could be integrated into existing permanently implanted structures, such as the common anastomotic flow couplers used in free flap surgeries [7] and stents [15]. The electronics in this research are designed with the intention of being incorporated into our prior work on stents that we used as energy harvesters to wirelessly power biomedical electronic implants in the peripheral vasculature [16]. An additional benefit of determining patency on the implant itself, rather than wirelessly transmitting data for external processing as done in our prior study [10], is to drastically reduce wireless channel usage and increase the number of permissible wireless bands that the device can operate within [17]. A single symbol need only to be transmitted representing the patency status at the end of the measurement period, compared to the 500 kBaud for continuous real-time external processing in our prior work.

## II. METHODOLOGIES

### A. Pig Bilateral Femoral Vein Blood Flow and Occlusion Dataset

In our previous study on anastomotic failure detection in the peripheral veins, we developed totally implantable wireless blood flow monitors to remotely monitor flow and occlusion states in the bilateral femoral veins in pigs [10]. We use the pig blood flow datasets generated from the prior study in this current research. There are

a total of eight blood flow data sets – four for each femoral vein; the entire dataset used in this research is from the same pig. Each dataset contains a “flow” and an “occlusion” component. The “flow” component corresponds to the blood flow signal recording in the femoral vein during normal flow conditions. The “occlusion” component corresponds to the blood flow signal recording while a ligature was tightened around the femoral vein to occlude flow completely.

Figure 1 shows the setup for collecting the pig blood flow data in our previous study. Ideally, there should only be a noise signal (i.e., the electrical noise in the measurement system) present during the occlusion measurement phase. However, physical movement, such as respiration, will introduce artifacts into the measured signal. During the surgery, a ventilator regulated the the pig’s breathing. Breathing is known to influence blood flow in the peripheral veins [18], and it is a necessary consequence of collecting blood flow data in anesthetized pigs.

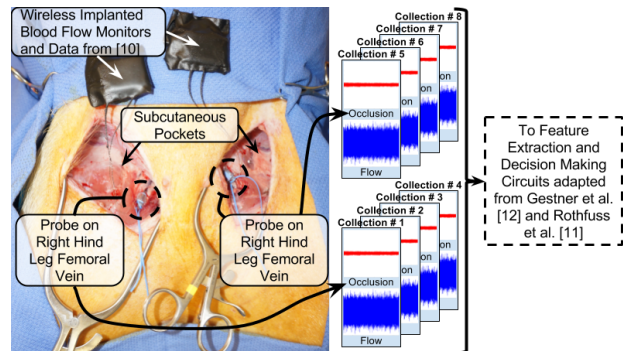


Fig. 1: Data collection setup to obtain “flow” and “occlusion” waveforms from our previous study [10]. The wireless implantable blood flow monitors are shown exposed for visualization purposes only; otherwise, the monitors are implanted within the subcutaneous pockets.

The 16 waveform segment (i.e., one “flow” and one “occlusion” for each of the eight datasets) stimulus files cumulatively represents 9 minutes and 22 seconds of collected blood flow data. The left hind-leg femoral vein dataset has 274 seconds of data, and the right hind-leg femoral vein dataset has 288 seconds of data. The “flow” and “occlusion” segment lengths for each dataset are equal (e.g., 30 seconds of “flow” data is accompanied by 30 seconds of “occlusion” data).

### B. Feature Extraction and Patency Discrimination

Our previous study on early-onset patency detection [11] was based on of the glass-break classifier developed

by Gestner et al. [12]. Their study used zero-crossing rate, high-band signal energy, and total signal energy features. Our study showed that using only total signal energy and zero-crossing rate (ZCR) features produced highly separable data. In this current study, we use Gestner et al.’s glass break classifier circuit adapted for classifying only the two features investigated in our previous study. The zero-crossing feature extraction circuit is from Gestner et al., and the total energy feature extraction circuit is from Twigg [19]. The ZCR circuit detects positive-to-negative zero-crossings, and the energy circuit detects the negative-going signal envelope.

Gestner et al.’s work was reported for the TSMC 0.35  $\mu\text{m}$  process. All circuits in this study are simulated in the IBM 130 nm CMOS process and designed for operation with a 1 V supply voltage, which is sufficient for integration into low-voltage wirelessly powered biomedical implants [20], [21], [22]. In preliminary calculations, the negative-going ZCR on the pig “flow” signals showed a ZCR frequency of  $1410 \pm 770$  Hz and a maximum and minimum frequency of 3025 Hz and 190 Hz, respectively. The peak negative-going amplitude reached 474.34 mV (i.e., mean peak amplitude is  $305.49 \pm 106.728$  mV). Therefore, we designed and benchmarked the feature extraction circuitry to operate within these limits.

Feature data are collected during a window period. The extracted feature signals are sampled and held to drive the inputs of the hyperplane decision circuitry for the duration of the window period. Because the eventual application of this technology is for wirelessly powered biomedical implants, we use the suggested window period, 200 ms, discussed in our prior study, which uses stents as energy harvesters in the peripheral vessels of the legs [16].

The resulting extracted feature data are projected onto a 2D plane and a separating hyperplane line is found to separate the “flow” and “occlusion” datasets. We use the Ho-Kashyap procedure used by both Gestner et al. [12] and in our previous study [11] to find the separating hyperplane line. We also use 10 k-fold cross-validation to prevent over-fitting to the data, and thus, there will be 10 separating hyperplane lines. The separating hyperplane line implemented by the classifier circuit is then matched to the average of the 10 k-fold separating hyperplane lines.

Figure 2 illustrates a block diagram showing the configuration and connections of the aforementioned circuits, as well as a detailed view of the hyperplane decision circuitry to illustrate its inner-workings. The “S/H” blocks refer to a sample and hold function asserted at the end of each window period – every 200 ms

(e.g., the “SH” in  $V_{\text{ENERGY,SH}}$  refers to the sampled and held energy feature voltage). In the hyperplane decision circuitry expanded view in the figure, the “ENERGY” and “ZCR” sections act as active current mirrors that clamp the drain of the NMOS transistor to the input (e.g.,  $V_{\text{ENERGY,SH}}$ ). The current through the NMOS transistor is set by a bias voltage, e.g.,  $V_{\text{bias,ENERGY}}$ . The “OTA” blocks are standard 5-transistor operational transconductance amplifiers (OTA) using PMOS inputs.  $I_{\text{OFF}}$  is the current when the  $V_{\text{ENERGY,SH}}$  and  $V_{\text{ZCR,SH}}$  voltages are at their maximum expected values, which results in minimum  $I_{\text{ZCR}}$  and  $I_{\text{ENERGY}}$  (i.e., supplied by suitable setting of  $V_{\text{bias,OFF}}$ ). When  $V_{\text{ENERGY,SH}}$  and  $V_{\text{ZCR,SH}}$  are below their maximum expected values,  $I_{\text{OUT}}$  increases.  $V_{\text{THRES}}$  sets a threshold for  $I_{\text{OUT}}$ ; below this threshold,  $V_{\text{PATENCY}}$  is low and above the threshold  $V_{\text{PATENCY}}$  is high. Adjusting  $V_{\text{THRES}}$  shifts the 2D hyperplane line and thus, the values of  $V_{\text{ENERGY,SH}}$  and  $V_{\text{ZCR,SH}}$  that result in a high or low  $V_{\text{PATENCY}}$ . A complete description of the hyperplane decision circuitry can be found in Gestner et al.’s work [12].

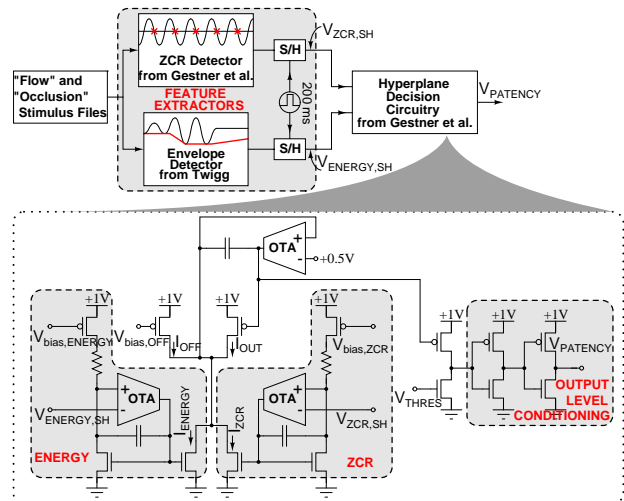


Fig. 2: Block diagram of the circuit components and their connections, the experimental setup, and a detailed view of the hyperplane decision circuitry. The ZCR detector is from Gestner et al., and the hyperplane decision circuitry was adapted from Gestner et al. [12]. The envelope detector is from Twigg [19].

### C. Experimental Setup and Data Collection

The following description refers to Figure 2. The experimental setup requires using the pig blood flow datasets as inputs to the simulated circuits. First, the sampled and held ZCR and energy feature values are

extracted from the datasets. Next, a separating hyperplane is found for the resulting feature value data using the Ho-Kashyap procedure. Then, the classifier circuit is tuned to match the computed separating hyperplane, and finally the pig blood flow dataset is input to the simulated circuits one more time, and the blood flow decision result from the classifier circuit is recorded from  $V_{\text{PATENCY}}$  in the figure. The same procedure was used in our prior study [11].

We pre-processed the datasets by using “flow” and “occlusion” segments that were void of obvious operator interference, such as tightening the ligature. Because the circuits’ supply voltage is 1 V, we clip the positive-going portion of the signals to 0.95 V, mimicking the action of a limiter circuit. Clipping the positive-going portion of the baseband blood flow signal does not affect the circuits, because the energy circuit detects only the negative-going signal envelope. A 700 mV DC bias is applied to the blood flow signals for the ZCR and energy circuits’ input stages.

### III. RESULTS

#### A. Feature Extraction Hardware Performance

In our previous study on automatic blood flow discrimination [11], the ZCR circuit accuracy showed a strong dependence on input signal amplitude. Whereas, the energy circuit showed little dependence on input signal frequency.

Figure 3 shows the ZCR feature extraction circuit performance. The circuit is benchmarked from 5 Hz to 4 kHz for various input signal amplitude ranges, beginning at 1 mV up through 700 mV. The preferred ZCR transfer function shows a linear frequency-to-voltage conversion. From the figure, we can see that signal amplitudes above approximately 20 mV result in accurate ZCR extraction. Meanwhile, signal amplitudes below 20 mV show significant ZCR inaccuracies. For example, low frequency low amplitude signal inputs show an extracted ZCR feature equivalent to high frequency input signals. The ZCR circuit in this study requires significantly lower input signal amplitude compared with our previous study implemented using discrete commercial off-the-shelf components [11]. Similar to Gestner et al.’s glass break feature extraction circuits [12], this ZCR circuit shows a non-ideal ZCR transfer function at the higher and lower frequency benchmarked ranges. The ZCR also shows that for occluded flow signals, where the number of zero-crossings will be dictated by noise bandwidth, the ZCR will output a high output voltage (i.e., due to low input amplitude).

Figure 4 shows the energy feature extraction circuit performance. The circuit is benchmarked from 1 mV to

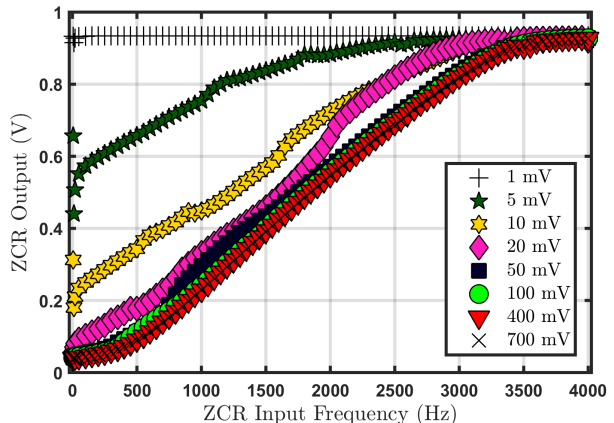


Fig. 3: ZCR circuit benchmark for various input voltage amplitudes ranging from 1 mV – 700 mV.

700 mV input signal amplitudes for signal frequencies from 5 Hz to 4 kHz. The ideal transfer function line is also shown in the figure. For signal frequencies 50 Hz and greater, we can see that the energy circuit tracks the input signal amplitude closely. Low frequency signals, regardless of input amplitude, are poorly represented at the circuit’s output. This can be explained by noting that the peak negative-going amplitude of frequencies below approximately twice the window period may not occur during the window period. Thus, frequencies below approximately 10 Hz will be poorly or irregularly represented by the energy circuit’s output. Upon further examination of the figure, one can see that the 5 Hz input frequency shows a near-quietest energy output voltage unless the input amplitude is large. This result can be explained by a combination of the effect of the envelope detector release time as well as when the peak negative-going amplitude occurs during the window capture period. Large signal amplitudes also show a deviation from ideal. In our dataset, the peak negative-going amplitude is 474.34 mV and the mean peak amplitude is 305.49 mV. For 50 Hz signal amplitudes of 0.3 V and 0.5 V, the deviation from ideal is 4.77% and 7.94%, respectively. For a 50 Hz 300 mV input amplitude, the deviation from ideal is about 4.70%.

#### B. Extracted Feature Data and Discriminative Hyperplane in Hardware

Figure 5(a) shows the extracted feature data from the feature extraction circuits along with each calculated K-fold hyperplane line, the average K-fold hyperplane line, and the extracted hyperplane line from the decision circuitry. The circuit hyperplane line was extracted in 5 mV

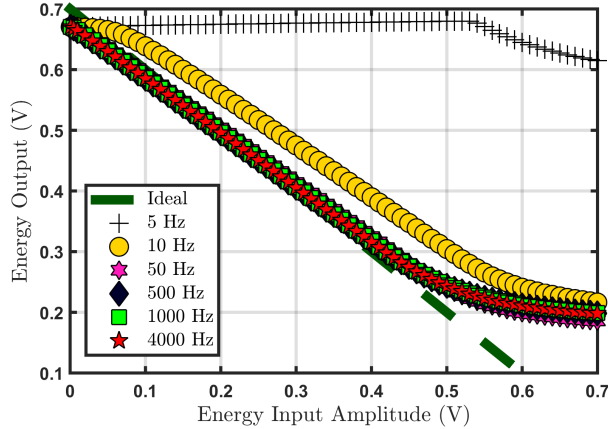
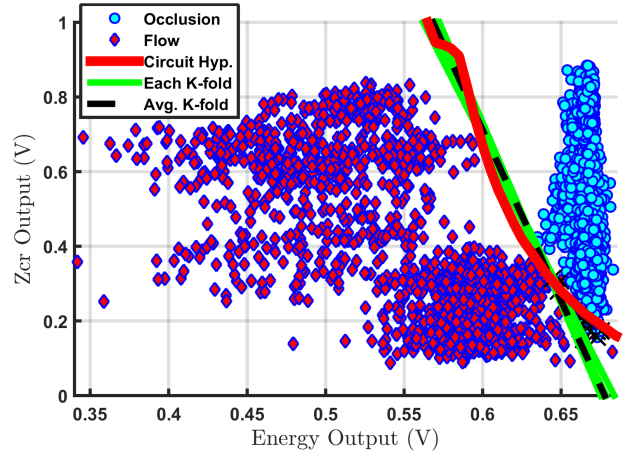


Fig. 4: Energy circuit benchmark for various input frequencies ranging from 5 Hz to 4 kHz.

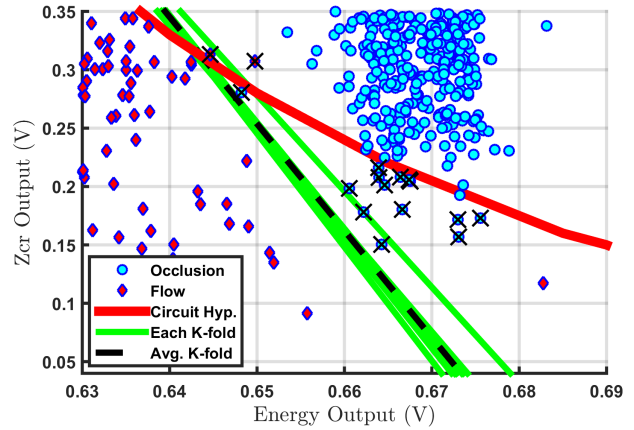
increments, and the static power consumption of the entire 1-V feature extraction and decision circuitry is  $8.715 \mu\text{W}$ . The calculated (i.e.,  $\sigma \pm \text{SE}$  where SE is the standard error defined as  $\frac{\sigma}{\sqrt{n}}$ ) sensitivity, specificity, and false-positive rate are  $99.93 \pm 0.07353\%$ ,  $99.78 \pm 0.1102\%$ , and  $0.2163 \pm 0.1102\%$ , respectively. Figure 5(b) shows a zoomed-in view where the feature data are very near the discriminating hyperplane line, where misclassifications occur. The misclassified feature data are marked with a black ‘ $\times$ ’. Fifteen “occlusion” feature data were misclassified. All but one are clustered in the zoomed-in view of figure 5(b). Two “flow” feature data are misclassified, leading to the simulated false-positive rate of 0.07275%. The simulated sensitivity and specificity are 99.45% and 99.93%, respectively.

#### IV. DISCUSSION

The high sensitivity, specificity, and low false-positive rate shown in this research, when using automatic flow classification on pig blood flow data collected from the peripheral veins, shows significantly lower false-positive rates than that found using the gold standard for free flap post-operative monitoring (i.e., as high as 31% [5]). Blood flow in the peripheral veins requires experienced personnel because the flow signal is difficult to distinguish from background noise [9]. This situation is shown clearly in the feature data in Figure 5. In the figure, a significant portion of the flow data are abutted nearly against the occlusion data, with merely 20 mV separating the two groups. This emphasizes the need for automatic classification as opposed to using experienced personnel. Also in the figure, more “occlusion” feature data are misclassified compared to the “flow” feature data. The likely causes for the misclassifications and the



(a)



(b)

Fig. 5: (a) Extracted energy and ZCR feature data from pig blood flow data showing extracted circuit discriminating hyperplane line. (b) Zoomed-in view of (a) showing misclassified feature data with a black ‘ $\times$ ’.

greater quantity of misclassified “occlusion” feature data are namely due to the pre-processing artifact removal procedure and the operating range of the hyperplane decision circuitry near its rails. The artifact removal process was done by hand, which of course is imperfect and can sometimes result in removing some desired signals as well as failing to remove undesirable signals, which leads to “flow” feature data appearing as “occlusion” feature data and vice versa. Also, the circuits used in this study were demonstrated in literature for an older CMOS process designed for higher voltages. We did not specifically re-design the circuits for low-voltage and wide input/output operating ranges, therefore we expected imperfect performance near the voltage rails, which manifested as the slightly curved discriminating

hyperplane line. This curve in the line erroneously places some “occlusion” feature data on the opposite side of the line (i.e., misclassification). Nearly the same curvature was observed in the discrete component implementation of the patency detector in our previous study [11].

Future studies should collect more blood flow data from many pigs across many vessels to determine if this classifier can be applied generally in the peripheral vasculature or if discriminating hyperplanes need to be generated *in situ*. Additionally, the feature data in Figure 5 can be mostly separated using the energy feature. However, our prior study on automatic classifiers for venous flow rates showed that very low flow rates that still fall within the normal range for a vessel will result in feature data, specifically for energy, that significantly overlaps that of the noise feature data [11]. For this case in our previous study, only by the addition of the ZCR feature is the separability improved between the flow and occlusion feature data groups.

The ideal blood flow monitor described by Smit et al. [14] outlined five key features: it should be easily deployable, the instrument output should be easily understood by inexperienced operators, it can be used at any site on the body, it does not impose discomfort for the patient, and it gives continuous and reliable monitoring at the monitoring site. Our study presents the first step towards satisfying all five of these features of an ideal monitor. Of all the blood flow monitoring modalities discussed by Smit et al., only the Laser Doppler, Near Infrared Spectroscopy (NIRS), and wired implantable Doppler probe and system come near to satisfying all of Smit et al.’s key features [13]. Laser Doppler, NIRS, and the wired implantable Doppler are all easily deployable and have simple outputs that can be generally easily understood (i.e., except the wired implantable Doppler which requires experienced personnel for venous flow monitoring) and can give continuous monitoring at the monitoring site. However, Laser Doppler and NIRS cannot be used to monitor deep vessels, such as in the case of buried free flaps [23], [7]; whereas, the wired implantable Doppler is well-suited for this application. While Laser Doppler and NIRS do not cause any patient discomfort, the wired implantable Doppler is invasive and can kink or tear the vessel if its monitoring wire is snagged. Notwithstanding, if the unreliability and hazards of the wired implantable Doppler, due to the transcutaneous tether, were to be eliminated, and the measurement output were easily interpretable for the peripheral venous flow applications, a Doppler blood flow monitoring technology stands to meet all of Smit et al.’s ideal blood flow monitor features.

In our prior study, we demonstrated patency detection

in the peripheral veins of pigs using wireless implantable blood flow monitors to improve on the shortcomings of the wired implantable Doppler system and probe [10]. However, the system still required an operator to compare readings to a baseline flow measurement, and additionally, the implant was still too bulky, leading to patient discomfort. It is for these reasons that we investigated automatic blood flow classification in our previous study [11] and the classifier’s performance in a monolithic embodiment in this current research. The advantage of a monolithic implantable blood flow monitor is that its small size significantly reduces patient discomfort, a feat that no other existing wireless implantable blood flow monitors can achieve because of their reliance on large commercial off-the-shelf (COTS) discrete components and batteries (i.e., see the review by Rothfuss et al. on wireless implantable blood flow monitors [13]). The smallest of the existing wireless blood flow monitors was reported in our previous study: 18 cm<sup>3</sup> including encapsulation and battery [10], while the next smallest reported in literature is 27 cm<sup>3</sup> by Yonezawa et al. [24]. As an integrated circuit, the electronics can be incorporated into existing implanted structures, such as anastomotic flow couplers [7] or stents [15], while only marginally increasing the implant size (e.g., the total implant device volume of our previous work was 18 cm<sup>3</sup> and 1.7 cm<sup>3</sup> without battery and without encapsulation).

The anastomotic flow coupler device is a popular and permanently implanted surgical tool used to mate and hold together the two vessel halves in an anastomosis procedure [25]. The anastomotic flow coupler often incorporates the Cook-Swartz wired implantable Doppler probe for precise placement and direct monitoring for the desired vessel [7]. The flow coupler’s high-density polyethylene body is bio-compatible and well-suited for encapsulating implanted electronics and a small implanted antenna, such as a loop antenna. Thus, an entirely implanted and percutaneously wirelessly powered blood flow monitor can be constructed to fit within the flow coupler, which stands to significantly improve the costly false-positive rates found using the transcutaneous wire tether blood flow monitor and flow coupler combination. In order to wirelessly power the implanted electronics through tissue, an external wireless antenna, such as a large loop antenna (e.g., several centimeters diameter [26]) transmits an electromagnetic field through tissue, which is then harvested by the implanted antenna. Significant power loss occurs in tissue (i.e., heating), and upper limits to the amount of power that can be transmitted through tissue for human safety (i.e., tissue heating) are imposed by the International Commission

on Non-Ionizing Radiation Protection (ICNIRP) [27] and the IEEE Standard C95.1-2005 [28]. Practical link gains between the external and implanted antennas are typically on the order of -10 to -30 dB, depending on a variety of factors such as implant depth, implant location, and antenna topology (e.g., dipole or loop antennas) [29]. Recent advances in ultra-small wireless power harvesting antennas for implanted devices using magnetodielectric cores in cubic millimeter loop antennas can safely provide over 600  $\mu\text{W}$  to a circuit at an 11 mm implant depth continuously at 300 MHz [30], near the 315 MHz ISM band investigated in our wireless stent study [16].

We estimate, from the following analysis of relevant literature, that an integrated circuit for wireless blood flow monitoring would require less than 2.2 mW available from the antenna. Using duty cycling can increase the implant depth and/or power available to the implant to meet safety regulations [31]. Highly efficient rectifiers for biomedical implants with efficiencies greater than 80% can maximize the power available to the implanted electronics [32]. The integrated circuit power consumption would be dominated by the piezoelectric transducers and their drive circuitry. Vilkomerson et al. demonstrated piezoelectric transducers requiring only 500  $\mu\text{W}$  of drive power from a digital inverter [33]. Assuming an example class B push-pull power amplifier transducer driver efficiency of 30%, the transducer and driver power consumption would be approximately 1.67 mW. Other monolithic portions suitable for integration into the implanted electronics could come from existing literature: 1.20  $\mu\text{W}$  for a 1-V 50 mA low-dropout regulator [34], 20.5  $\mu\text{W}$  for the low-noise amplifier front-end designed for ultrasonic transducers [35], and 1.5  $\mu\text{W}$  for baseband amplification and low-pass filtering [36]. The simulated quiescent current consumption of the feature extraction and discriminating hyperplane decision circuitry in this research, adapted from Gestner et al. [12], is 8.715  $\mu\text{A}$  from a 1-V supply. Comparatively, Gestner et al.'s glass break detector consumed 20  $\mu\text{A}$  in a TSMC 0.35  $\mu\text{m}$  process (i.e., supply voltage was not specified). Thus, the total power consumption of the electronics (i.e., neglecting rectifier efficiency) is approximately 1.7 mW.

If the aforementioned example integrated device were to be incorporated within the wireless stent energy harvesters for the peripheral vasculature from our prior study [16], 6.687 mW of power would be available from the antenna (i.e., using conjugate matching) at a 4.36 cm implant depth (i.e., 0.19 cm 2.1 cm fat, and 2.07 cm muscle), and a 20% power-on duty cycle (i.e., 200 ms window length). This would mean that the implanted wirelessly powered blood flow meter (i.e., requires 2.2 mW) could easily be powered far beyond

the maximum monitoring depths of NIRS (i.e., 20 mm [37]) and Laser Doppler (i.e., 8 mm [38]), via [14]. A future study should investigate methods to powering a miniature implantable antenna incorporated into a flow coupler device to determine the power available for implanted electronics in buried flap cases. A miniature monitoring device that can be incorporated into existing implantable devices that significantly reduces bioburden and deployment barriers, automatically determines vessel patency, can be operated below the operational depths of the nearest competing technologies, and can be powered continuously without reliability concerns (i.e., due to the transcutaneous wire) positions itself closer to the ideal monitor described by Smit et al. than any other reported device.

## V. CONCLUSION

This paper demonstrated the performance of a hardware-only blood flow classifier intended for integration within a biomedical implant. We validated the hardware-only feature extraction and classification circuitry in SPICE simulations using the IBM 130 nm CMOS process for a 1-V supply voltage using real pig blood flow data in the bilateral femoral veins, which often require experienced personnel to detect occlusions. Our results show that a high sensitivity, specificity, and low false-positive rate are achievable using automatic hardware-only patency classification on real pig blood flow data in a 200 ms window size at a low quiescent power. These results suggest that automatic patency classifiers incorporated as part of a wirelessly-powered biomedical implant will be able to detect the presence and loss of venous flow for free flap surgeries without experienced operators.

## REFERENCES

- [1] F. Hölzle, A. Rau, D. Loeffelbein, T. Mücke, M. Kesting, and K.-D. Wolff, "Results of monitoring fasciocutaneous, myocutaneous, osteocutaneous and perforator flaps: 4-year experience with 166 cases," *International Journal of Oral and Maxillofacial Surgery*, vol. 39, no. 1, pp. 21–28, 2010.
- [2] K. Z. Paydar, S. L. Hansen, D. S. Chang, W. Y. Hoffman, and P. Leon, "Implantable venous Doppler monitoring in head and neck free flap reconstruction increases the salvage rate," *Plastic and Reconstructive Surgery*, vol. 125, no. 4, pp. 1129–1134, 2010.
- [3] S. S. Kroll, M. A. Schusterman, G. P. Reece, M. J. Miller, G. R. Evans, G. L. Robb, and B. J. Baldwin, "Timing of pedicle thrombosis and flap loss after free-tissue transfer," *Plastic and Reconstructive Surgery*, vol. 98, no. 7, pp. 1230–1233, 1996.
- [4] X. F. Ling and X. Peng, "What is the price to pay for a free fibula flap? a systematic review of donor-site morbidity following free fibula flap surgery," *Plastic and Reconstructive Surgery*, vol. 129, no. 3, pp. 657–674, 2012.
- [5] R. E. H. Ferguson Jr and P. Yu, "Techniques of monitoring buried fasciocutaneous free flaps," *Plastic and Reconstructive Surgery*, vol. 123, no. 2, pp. 525–532, 2009.

- [6] J. P. Fischer, B. Sieber, J. A. Nelson, E. Cleveland, S. J. Kovach, L. C. Wu, S. Kanchwala, and J. M. Serletti, "Comprehensive outcome and cost analysis of free tissue transfer for breast reconstruction: an experience with 1303 flaps," *Plastic and Reconstructive Surgery*, vol. 131, no. 2, pp. 195–203, 2013.
- [7] T. Zhang, D. Dyalram-Silverberg, T. Bui, J. F. Caccamese, and J. E. Lubek, "Analysis of an implantable venous anastomotic flow coupler: experience in head and neck free flap reconstruction," *International Journal of Oral and Maxillofacial Surgery*, vol. 41, no. 6, pp. 751–755, 2012.
- [8] W. M. Swartz, R. Izquierdo, and M. J. Miller, "Implantable venous Doppler microvascular monitoring: Laboratory investigation and clinical results," *Plastic and Reconstructive Surgery*, vol. 93, no. 1, pp. 152–163, 1994.
- [9] A. I. Galeandro, G. Quistelli, P. Scicchitano, M. Gesualdo, A. Zito, P. Caputo, R. Carbonara, G. Galgano, F. Ciciarello, S. Mandolesi, C. Franceschi, and M. M. Ciccone, "Doppler ultrasound venous mapping of the lower limbs," *Vascular Health and Risk Management*, vol. 8, p. 59, 2012.
- [10] M. A. Rothfuss, N. G. Franconi, J. V. Unadkat, M. L. Gimbel, A. Star, M. H. Mickle, and E. Sejdic, "A system for simple real-time anastomotic failure detection and wireless blood flow monitoring in the lower limbs," *IEEE Journal of Translational Engineering in Health and Medicine*, vol. 4, pp. 1–15, 2016.
- [11] M. A. Rothfuss, N. G. Franconi, A. Star, M. Akcakaya, M. L. Gimbel, and E. Sejdic, "Automatic early-onset free flap failure detection for implantable biomedical devices," *IEEE Transactions on Biomedical Engineering*, 2017, Submitted.
- [12] B. Gestner, J. Tanner, and D. Anderson, "Glass break detector analog front-end using novel classifier circuit," in *2007 IEEE International Symposium on Circuits and Systems*. IEEE, 2007, pp. 3586–3589.
- [13] M. A. Rothfuss, J. V. Unadkat, M. L. Gimbel, M. H. Mickle, and E. Sejdic, "Totally implantable wireless ultrasonic Doppler blood flowmeters: Toward accurate miniaturized chronic monitors," *Ultrasound in Medicine & Biology*, vol. 43, no. 3, pp. 561–578, 2017.
- [14] J. M. Smit, C. J. Zeebregts, R. Acosta, and P. M. N. Werker, "Advancements in free flap monitoring in the last decade: a critical review," *Plastic and Reconstructive Surgery*, vol. 125, no. 1, pp. 177–185, 2010.
- [15] E. Y. Chow, Y. Ouyang, B. Beier, W. J. Chappell, and P. P. Irazoqui, "Evaluation of cardiovascular stents as antennas for implantable wireless applications," *IEEE Transactions on Microwave Theory and Techniques*, vol. 57, no. 10, pp. 2523–2532, 2009.
- [16] M. A. Rothfuss, N. G. Franconi, K. N. Bocan, J. V. Unadkat, M. L. Gimbel, M. H. Mickle, and E. Sejdic, "Can we wirelessly and safely monitor peripheral artery disease?" *IEEE Transactions on Biomedical Engineering*, 2017, Submitted.
- [17] S. Mandal and R. Sarpeshkar, "Power-efficient impedance-modulation wireless data links for biomedical implants," *IEEE Transactions on Biomedical Circuits and Systems*, vol. 2, no. 4, pp. 301–315, Dec 2008.
- [18] W. Brant, *The Core Curriculum, Ultrasound*, ser. LWW Doody's all reviewed collection. Lippincott Williams & Wilkins, 2001.
- [19] C. M. Twigg, "Floating gate based large-scale field-programmable analog arrays for analog signal processing," Ph.D. dissertation, Georgia Institute of Technology, 2006.
- [20] A. P. Chandrakasan, N. Verma, and D. C. Daly, "Ultralow-power electronics for biomedical applications," *Annual Review of Biomedical Engineering*, vol. 10, pp. 247–274, 2008.
- [21] A. C. W. Wong, G. Kathiresan, C. K. T. Chan, O. Eljamaly, O. Omeni, D. McDonagh, A. J. Burdett, and C. Toumazou, "A 1 v wireless transceiver for an ultra-low-power soc for biotelemetry applications," *IEEE Journal of Solid-State Circuits*, vol. 43, no. 7, pp. 1511–1521, 2008.
- [22] X. Zou, X. Xu, L. Yao, and Y. Lian, "A 1-v 450-nw fully integrated programmable biomedical sensor interface chip," *IEEE Journal of Solid-State Circuits*, vol. 44, no. 4, pp. 1067–1077, 2009.
- [23] J. J. Rosenberg, B. D. Fornage, and P. M. Chevray, "Monitoring buried free flaps: limitations of the implantable Doppler and use of color duplex sonography as a confirmatory test," *Plastic and Reconstructive Surgery*, vol. 118, no. 1, pp. 109–113, 2006.
- [24] Y. Yonezawa, T. Nakayama, I. Ninomiya, and W. Caldwell, "Radio telemetry directional ultrasonic blood flowmeter for use with unrestrained animals," *Medical and Biological Engineering and Computing*, vol. 30, no. 6, pp. 659–665, 1992.
- [25] S. J. Kempton, S. O. Poore, J. T. Chen, and A. M. Afifi, "Free flap monitoring using an implantable anastomotic venous flow coupler: Analysis of 119 consecutive abdominal-based free flaps for breast reconstruction," *Microsurgery*, vol. 35, no. 5, pp. 337–344, 2015.
- [26] M. Mark, T. Björninen, L. Ukkonen, L. Sydänheimo, and J. M. Rabaey, "SAR reduction and link optimization for mm-size remotely powered wireless implants using segmented loop antennas," in *2011 IEEE Topical Conference on Biomedical Wireless Technologies, Networks, and Sensing Systems*. IEEE, 2011, pp. 7–10.
- [27] I. Guideline, "Guidelines for limiting exposure to time-varying electric, magnetic, and electromagnetic fields (up to 300 GHz)," *Health Phys*, vol. 74, no. 4, pp. 494–522, 1998.
- [28] "IEEE standard for safety levels with respect to human exposure to radio frequency electromagnetic fields, 3 kHz to 300 GHz," *IEEE Std C95.1-2005 (Revision of IEEE Std C95.1-1991)*, pp. 1–238, April 2006.
- [29] K. N. Bocan, M. H. Mickle, and E. Sejdic, "Tissue variability and antennas for power transfer to wireless implantable medical devices," *IEEE Journal of Translational Engineering in Health and Medicine*, 2017.
- [30] E. Moradi, T. Björninen, L. Sydänheimo, J. M. Carmena, J. M. Rabaey, and L. Ukkonen, "Measurement of wireless link for brain-machine interface systems using human-head equivalent liquid," *IEEE Antennas and Wireless Propagation Letters*, vol. 12, pp. 1307–1310, 2013.
- [31] E. Y. Chow, "Wireless miniature implantable devices and ASICs for monitoring, treatment, and study of glaucoma and cardiac disease," Ph.D. dissertation, Purdue University, 2009.
- [32] M. Zargham and P. G. Gulak, "A 0.13  $\mu\text{m}$  CMOS integrated wireless power receiver for biomedical applications," in *2013 Proceedings of the 39th European Solid-State Circuits Conference*. IEEE, 2013, pp. 137–140.
- [33] D. Vilkomerson and T. Chilipka, "Implantable Doppler system for self-monitoring vascular grafts," in *2004 IEEE Ultrasonics Symposium*, vol. 1. IEEE, Aug 2004, pp. 461–465.
- [34] M. Ho and K. N. Leung, "Dynamic bias-current boosting technique for ultralow-power low-dropout regulator in biomedical applications," *IEEE Transactions on Circuits and Systems II: Express Briefs*, vol. 58, no. 3, pp. 174–178, 2011.
- [35] E. R. Björsvik, "Design of energy efficient low noise amplifiers in 40 nm bulk CMOS and 28 nm FD-SOI for intravascular ultrasound imaging," 2014.
- [36] V. Chaturvedi and B. Amrutur, "An area-efficient noise-adaptive neural amplifier in 130 nm CMOS technology," *IEEE Journal on Emerging and Selected Topics in Circuits and Systems*, vol. 1, no. 4, pp. 536–545, 2011.
- [37] A. Repež, D. Oroszy, and Z. M. Arnež, "Continuous postoperative monitoring of cutaneous free flaps using near infrared spectroscopy," *Journal of Plastic, Reconstructive & Aesthetic Surgery*, vol. 61, no. 1, pp. 71–77, 2008.
- [38] F. Hölzle, D. J. Loeffelbein, D. Nolte, and K.-D. Wolff, "Free flap monitoring using simultaneous non-invasive laser Doppler flowmetry and tissue spectrophotometry," *Journal of Cranio-Maxillofacial Surgery*, vol. 34, no. 1, pp. 25–33, 2006.